

Diamond Magnetometry and Gradiometry Towards Subpicotesla dc Field Measurement

Chen Zhang,^{1,*} Farida Shagieva², Matthias Widmann,¹ Michael Kübler¹, Vadim Vorobyov,¹ Polina Kapitanova³, Elizaveta Nenasheva,⁴ Ruth Corkill,⁵ Oliver Rhrle,⁵ Kazuo Nakamura⁶, Hitoshi Sumiya⁷, Shinobu Onoda⁸, Junichi Isoya,⁹ and Jörg Wrachtrup^{1,†}

¹*3rd Institute of Physics, University of Stuttgart, Pfaffenwaldring 57, Stuttgart 70569, Germany*

²*TTI GmbH / TGZ SQUTEC, Nobelstraße 15, Stuttgart 70569, Germany*

³*Department of Physics and Engineering, ITMO University, Saint Petersburg 197101, Russia*

⁴*Giricond Research Institute, Ceramics Co. Ltd., Saint Petersburg 194223, Russia*


⁵*Institute for Modelling and Simulation of Biomechanical Systems, Pfaffenwaldring 5a, Stuttgart 70569, Germany*

⁶*Leading-Edge Energy System Research Institute, Fundamental Technology Department, Tokyo Gas Co. Ltd., Yokohama 230-0045, Japan*

⁷*Advanced Materials Laboratory, Sumitomo Electric Industries, Ltd., Itami 664-0016, Japan*

⁸*Takasaki Advanced Radiation Research Institute, National Institutes for Quantum and Radiological Science and Technology, Takasaki 370-1292, Japan*

⁹*Faculty of Pure and Applied Sciences, University of Tsukuba, Tsukuba 305-8573, Japan*

 (Received 2 January 2021; revised 10 April 2021; accepted 8 June 2021; published 30 June 2021)

Nitrogen-vacancy (N-V) centers in diamond have developed into a powerful solid-state platform for compact quantum sensors. However, high-sensitivity measurements usually come with additional constraints on the pumping intensity of the laser and the pulse control applied. Here, we demonstrate high-sensitivity N-V-ensemble-based magnetic field measurements with low-intensity optical excitation. Direct current magnetometry methods such as continuous-wave optically detected magnetic resonance and continuously excited Ramsey measurements combined with lock-in detection are compared to achieve an optimization. Gradiometry is also investigated as a step towards unshielded measurements of unknown gradients. The magnetometer demonstrates a minimum detectable field of 0.3–0.7 pT in a 73-s measurement when a flux guide with a sensing dimension of 2 mm is applied, corresponding to a magnetic field sensitivity of 2.6–6 pT/ $\sqrt{\text{Hz}}$. Combined with our previous efforts on diamond ac magnetometry, the diamond magnetometer is promising for performing wide-bandwidth magnetometry with picotesla sensitivity and a cubic-millimeter sensing volume under ambient conditions.

DOI: [10.1103/PhysRevApplied.15.064075](https://doi.org/10.1103/PhysRevApplied.15.064075)

I. INTRODUCTION

Quantum sensors have made extraordinary progress in sensitivity, precision, bandwidth, and spatial and temporal resolution over the past years [1–4]. They have enabled measurements with cutting-edge performance of various physical quantities, including frequency standards, magnetic and electric fields, temperatures, rotations, and gravitational fields [5–10]. Among all the efforts dedicated to advancing the measurement limits, measurements of static or low-frequency magnetic fields (dc magnetometry) are the most important ones [11,12]. dc magnetometry allows a wide range of applications in fields such as medical and material science [13–18].

Highly sensitive dc magnetometry techniques have been developed across various platforms, with sensitivities from femtoteslas to nanoteslas [18–22]. Superconducting quantum interference devices held the sensitivity record of 1 fT/ $\sqrt{\text{Hz}}$ with a spatial resolution of a few centimeters [23] until atomic-vapor cells achieved a record sensitivity of 160 aT/ $\sqrt{\text{Hz}}$ in a volume of 0.45 cm³ with gradiometry measurement [3,24]. However, there are still technical challenges concerning further miniaturization without compromising such high sensitivities [25]. On the other hand, the nitrogen-vacancy center in diamond has evolved into a competitive room-temperature platform for magnetometry with its exceptional spatial resolution, dynamic range, and sensitivity [2,26]. With neither cryogenic nor heating requirements in operation, the sensor head can be reduced to the size of the diamond itself, i.e., less than 1 mm³, while still keeping picotesla

*c.zhang@pi3.uni-stuttgart.de

†j.wrachtrup@pi3.uni-stuttgart.de

sensitivity [2]. Furthermore, the $N-V^-$ centers can be operated in bias fields from zero to a few tesla [27,28]. In 2016, a $15\text{-pT}/\sqrt{\text{Hz}}$ dc sensitivity was demonstrated, and a magnetometer was successfully applied to sense neuron activity in a marine worm [29]. Such high-sensitivity $N-V^-$ magnetometry usually requires a high excitation laser power. Recently, by applying a flux concentrator (FC) to enhance the local magnetic field by more than a factor of 200, the dc sensitivity has been improved from 300 to $0.9\text{ pT}/\sqrt{\text{Hz}}$, while the excitation laser power is significantly lower than the power commonly used in high-sensitivity measurements [30]. Although this improvement in sensitivity comes at the price of reduced spatial resolution, the device still has a cubic-centimeter sensing volume with a significantly higher dynamic range compared with optically pumped magnetometers (OPMs).

In this paper, we present dc magnetometry and gradiometry with a diamond volume of $(0.5\text{ mm})^3$, which contains $N-V^-$ -center ensembles with a minimum optically detected magnetic resonance (ODMR) linewidth of 28 kHz and a long dephasing time of $8.5\text{ }\mu\text{s}$. With an excitation laser power below 100 mW, multiple methods of diamond dc magnetometry are investigated. Pulsed schemes with continuous excitation and readout are demonstrated with a better sensitivity potential than optimized continuous-wave ODMR (cw ODMR) measurements. On the other hand, we also show that cw ODMR measurements driving both hyperfine and double-resonance (DR) transitions demonstrate an optimized sensitivity close to that of Ramsey measurements with the same low-power laser excitation. We present a measurement showing a minimum detectable field of 2–3 pT within a bandwidth of 0–200 Hz in a 73-s measurement time, and the 1-Hz normalized noise spectral density is $17\text{ pT}/\sqrt{\text{Hz}}$. We also present a gradiometry measurement, showing a minimum detectable differential field noise of 4–6 pT with a 73-s measurement time. Furthermore, when a ferrite flux guide (FG) is applied, the measured minimum detectable field goes down to the subpicotesla range of 0.3–0.7 pT over the above bandwidth, corresponding to a sensitivity level of $2.6\text{--}6\text{ pT}/\sqrt{\text{Hz}}$.

II. EXPERIMENT

A. Experimental setup and methods

The optimization of the sensitivity of diamond magnetometry has been reviewed in detail recently [31]. $N-V^-$ magnetometry is based on the Zeeman shift of the ground-state sublevels of the $N-V^-$ center. The $S = 1$ spin can be initialized by green-laser pumping through the intersystem crossing (ISC) process, and the triplet ground state can be resonantly driven by microwaves (MW). The typical way of measuring the Zeeman shift is to detect the fluorescence change induced by the difference in the sublevel populations. The intrinsic noise of the magnetometer can be defined as $\delta B = \sigma(t)/(dS/dB)$, where $\sigma(t)$ is the detected

noise floor excluding external field noise, and the scalar factor dS/dB is the change in the signal dS occurring per magnetic field change dB . In $N-V^-$ -ensemble magnetometry, the characteristics of the noise are essentially determined by the characteristics of the $N-V^-$ ensemble. The minimum detectable field scales with the sensing volume and the measurement time [4]. In this paper, we apply an optimized diamond sample with a narrow-linewidth $N-V^-$ ensemble, and focus mainly on compromising between the signal level and the technical noise and feasibility.

Figure 1 shows the experimental setup and the energy-level diagram for the photodynamic and spin-kinetic simulations [32]. A magnetic shield cube entirely encloses the setup to attenuate the magnetic field noise in the laboratory. An optical compound parabolic concentrator (CPC) is used for high fluorescence collection efficiency, which exceeds 60% [4]. The dielectric resonator antenna generates a uniform driving MW field for the $N-V^-$ ensemble [33]. We investigate the performance of a gradiometer by constructing two identical diamond sensors, as shown in Fig. 1(b). A loop antenna is applied in the reference channel. In order to test the sensitivity enhancement provided by the FG, a ferrite rod (MN60) is placed between the diamond and the coil applying the test field, as shown in Fig. 1(c). The diameter of the FG tip is 2 mm. The gap between the FG and the diamond is roughly 1 mm, limited by the CPC lens structure. The FG-assisted enhancement could be higher with a decreased distance to the diamond.

One of the most critical techniques for sensitive measurements is lock-in detection to avoid low-frequency $1/f$ noise. Figure 2(a) shows the typical cw ODMR output from a lock-in amplifier (LIA), with the spin transitions of the $N-V^-$ centers driven by a modulated MW field. The MW

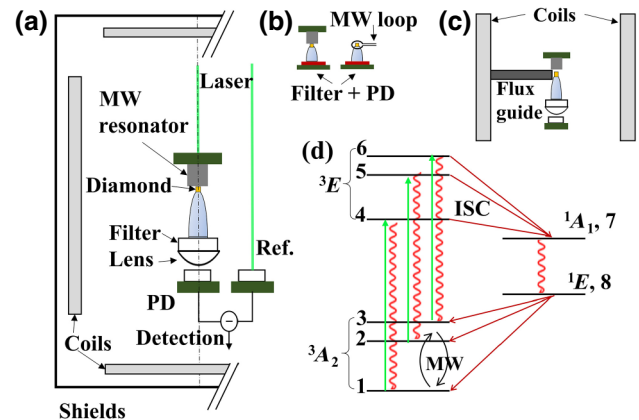


FIG. 1. (a) The experimental setup is installed in a magnetic field shield for high-sensitivity measurements. PD, photodetector. (b) Two identical diamond sensors are constructed to measure the noise floor in the gradiometer configuration. The reference channel uses a loop antenna. (c) A flux guide is placed between the diamond and a coil for enhancement of the magnetic field sensitivity. (d) Energy diagram of $N-V^-$ center.

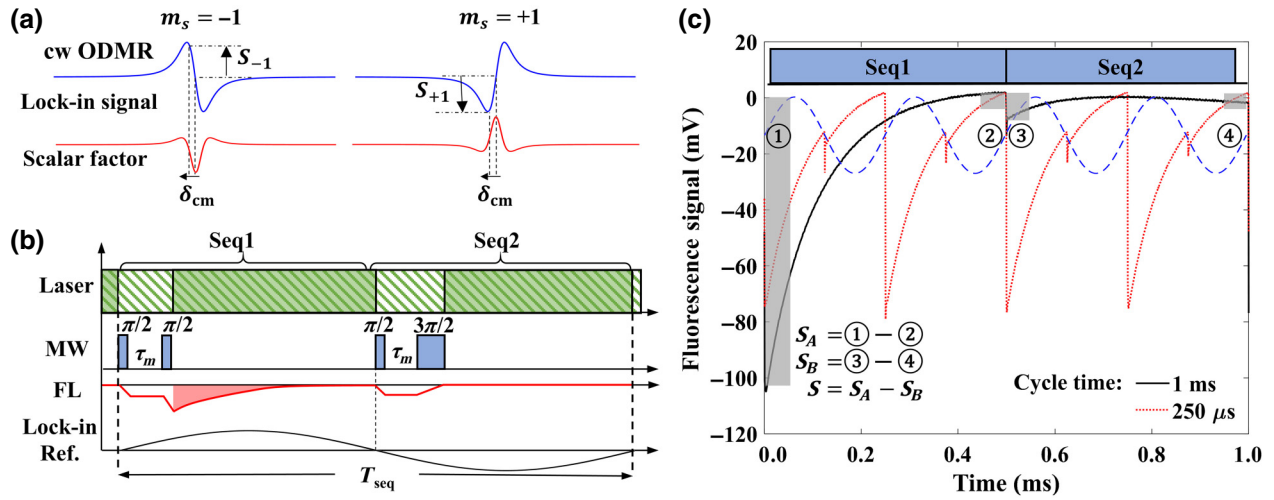


FIG. 2. (a) Lock-in-detected cw ODMR signal profile and the corresponding scalar factor. δ_{cm} is a common-mode line shift of the two resonant lines. S_{-1} and S_{+1} are the corresponding signals, with the same amplitude but different signs. (b) A continuously excited Ramsey (CE Ramsey) sequence is used to promote the cw ODMR measurement. The blocks of solid color labeled “Laser” depict the laser pulses used in a traditional Ramsey measurement, while in the CE Ramsey method the laser is continuously applied in all the time bins, as shown by the cross-hatched area. The curve labeled FL (red line) depicts the fluorescence signal when the external field is zero. The signal in the time bins corresponding to the solid laser blocks is a valid signal for magnetic field sensing, as shown by the shaded area for Seq1. The remaining signal becomes negligible when $\tau_m \ll T_{seq}$, which can be seen in (c), which shows the fluorescence readout for cycle times $T_{seq} = 1$ ms (black solid curve) and 250 μ s (red dotted curve). The Seq1 and Seq2 blocks on the top correspond to the signal for the 1-ms cycle. The figure shows both the conventional readout method (shown for the 1-ms-cycle signal) and the lock-in readout method (shown for the 250- μ s-cycle signal). The signals in the gray areas are calculated following the equations shown in the figure for conventional readout. For lock-in detection, the demodulation reference is applied according to the dashed sinusoidal line.

modulation phases are of opposite sign for the $|0\rangle \rightarrow |+1\rangle$ and $|0\rangle \rightarrow |-1\rangle$ transitions [30]. Thus, the signals S_{-1} and S_{+1} , which are induced by the common-mode line shift δ_{cm} , have the same amplitude but different signs. The common-mode line shifts are induced mainly by thermal fluctuations. By tracking the resonance lines in the case of larger magnetic fields, one can maintain the maximum scalar factor and the linearity of the system.

Figure 2(b) shows a Ramsey sequence as an example of a pulsed measurement sequence obtained using a LIA, while Fig. 2(c) depicts the signal dynamics together with the acquisition methods. In the Ramsey measurements used up to now [2], the laser is turned off during the field acquisition time τ_m . The fluorescence signal is therefore gated and appears as pulses. However, the signal dS amounts to only a few percent of the overall signal. The background fluorescence consumes most of the bits of the digitizer when normal photodetectors are used. An alternative could be to use a balanced detector. However, when the two channels are not perfectly balanced due to stability reasons, the remaining pulsed signals still induce overshoot and delay errors in the electronics. Besides, the thermal dynamics induced by the laser pulses contributes to additional errors in the measurement. Thus, we modify the sequence to a continuous excitation mode with the

laser turned on all the time, as shown in Fig. 2(b). The fluorescence during τ_m and the time of the MW pulses can be neglected due to the low repolarization rate under the low-power laser excitation. One of the apparent advantages of using continuous excitation is the simplicity of the laser optics; e.g., an optical switch is no longer required even for MW pulsed measurements. By simply applying ac coupling to the digitizer, any background signal can be removed without any noise induced by the pulsed signals. Moreover, the photodetectors do not need a wide bandwidth under continuous excitation for the high-dynamic-pulse signals, so that the gain can be increased for a better signal-to-noise ratio (SNR). Heating fluctuations induced by the pulsed laser can be removed, and the thermal stability can be improved by monitoring the laser-power drift for compensation. The disadvantage is that the laser repolarizes the $N-V$ centers during τ_m , which reduces dS . In a quantitative treatment of the measurements, this is treated as a lower polarization rate, i.e., it reduces the contrast a little but does not induce an error in the phase accumulation. We would like to note that a continuous excitation mode can also be applied in other pulsed measurement schemes, such as Hahn-echo and high-order dynamical decoupling sequences. The black curve in Fig. 2(c) is the fluorescence signal for a cycle time of 1 ms. The labeled grey areas and

the inset formulas describe the acquisition method that was used in previous work [4].

For the sensitivity calculation using the signal S , we need to consider the scaling of the noise with a factor $\sqrt{T_{\text{seq}}/\Delta t}$, where T_{seq} is the sequence time and Δt is the total acquisition time. On the other hand, the lock-in detection is equivalent to a method in which S_A and S_B are the averaged signal levels of each half reference cycle and S is the amplitude of the entire cycle. The LIA integrates all the detected fluorescence, so that there is no acquisition-time intermittency, which would deteriorate the sensitivity. Therefore, the measured minimum detectable field, i.e., the shot noise of the Ramsey measurement, can be expressed as [2,31]

$$\delta B_{\text{Ramsey}} = \frac{\hbar}{g\mu_B} \frac{1}{C_{\text{det}}\sqrt{N}\tau_m t} \sqrt{\frac{T_{\text{seq}}}{\tau_m}}, \quad (1)$$

where τ_m is optimized with respect to the dephasing time T_2^* , C_{det} is the detected contrast, N is the number of photons collected per measurement, and t is the measurement time. Experimentally, N can be estimated from the photon detection rate $R = N/T_{\text{seq}}$. The sensitivity is calculated as $\eta = \delta B\sqrt{t}$. The equation calculates the shot noise without explicitly including the photon detection efficiency. When the laser power does not saturate the N-V ensemble, as in our case of low optical pumping, the collected photon rate is also related to the pumping power. In Fig. 2(c), the dotted line shows the fluorescence signal for a 250- μ s cycle time, and the dashed line shows the corresponding lock-in reference. When the time duration of each part of the sequence is significantly shorter than the repolarization time of the spins, the contrast is reduced dramatically due to insufficient repolarization. The contrast increases with higher pumping power when the polarization time T_p is fixed. In this case, T_{seq} can be made shorter to make the magnetometer more sensitive.

However, we will see later that a laser power of watts is required to get a significant improvement in sensitivity. In order to make it clearer in the model, we denote the contrast by $C(P, T_p)$, where P is the applied laser power. Note that the contrast also decays with the phase factor $\exp(-\tau_m/T_2^*)$, so that the detected contrast is given by $C_{\text{det}} = C(P, T_p) \exp(-\tau_m/T_2^*)$. Meanwhile, improving the laser power leads to higher fluorescence signals due to a greater number of optical cycles, and it also contributes to a linear rise in the laser noise. It becomes rather complicated to get better sensitivity in practice then. Thus, we optimize the system with a fixed low laser power to make a trade-off between the technical noise floor and the signal contrast, which both decrease with higher demodulation frequency.

B. Optimization of parameters

Among all the schemes for diamond dc magnetometry, Ramsey magnetometry is one of the most sensitive

methods. However, its practical sensitivity suffers from technical limitations. For example, an enormous laser power is needed for the initialization of the spin ensembles. This brings heating problems and extra noise with it. In contrast, cw ODMR is a method that can be easily implemented with a low laser power. In the following, we first analyze the sensitivity of the cw ODMR method and the optimal laser and MW parameters. Then, Ramsey magnetometry is investigated based on the same laser power. The shot noise measured by the cw ODMR method is described as [34]

$$\delta B_{\text{cw}} = P_F \frac{\hbar}{g\mu_B} \frac{\nu(s, \Omega_R)}{C_{\text{det}}(s, \Omega_R)\sqrt{Rt}}. \quad (2)$$

Here P_F is a lineshape-dependent factor, which is 0.77 for the Lorentzian line profile used in the present work. The critical parameters for experimental optimization are the linewidth ν and the contrast C_{det} , which are dependent on the Rabi frequency Ω_R and the ratio of the applied laser power to the saturation power, s . Figure 3(a) plots the dependence of the sensitivity on these parameters. T_1 and T_2^* used in the calculation are 6 ms and 8.5 μ s, respectively. The optimized magnetometry parameters are $\Omega_R = 23$ kHz and $s = 3 \times 10^{-4}$. The shot-noise-limited sensitivity is 2.86 pT/ $\sqrt{\text{Hz}}$ for the signal of a single hyperfine line. By driving the three hyperfine lines, the contrast can ideally be increased by 3 times. However, the contrast enhancement factor in the experiment is smaller because of reasons such as the near-resonant driving induced by the multiple MW frequencies. This effect could be limited by applying weak MW driving. In our experiments, the contrast enhancement factor is 2.67. The scalar factor is further improved by DR driving, and the experimental enhancement factor is 1.3 times. Therefore, the sensitivity limit of the cw ODMR method is expected to be 0.82 pT/ $\sqrt{\text{Hz}}$ when all the hyperfine lines are driven and DR driving is used. The estimated sensitivity limit based on the calculations shown in Fig. 3(a) does not include the influence of MW modulation. MW modulation reduces the contrast due to the frequency response of the magnetometer, depending on the optical pumping. In the following, we discuss the magnetometry parameters near the optimized optical pumping power.

In order to obtain an optimized SNR, the collected fluorescence emission power should be on the order of a milliwatt, with a value roughly 3×10^{-4} times lower than the saturation laser power. In order to avoid applying an unnecessarily high laser power, the excitation power is optimized by comparing the experimental pumping rate with a simulation of the excitation kinetics. For a fluorescence emission rate of 66 MHz [35,36], the optimized pumping rate is estimated to be around 0.02 MHz. This parameter underestimates the pumping rate due to neglecting charge-state conversion in the kinetics [37,38]. We

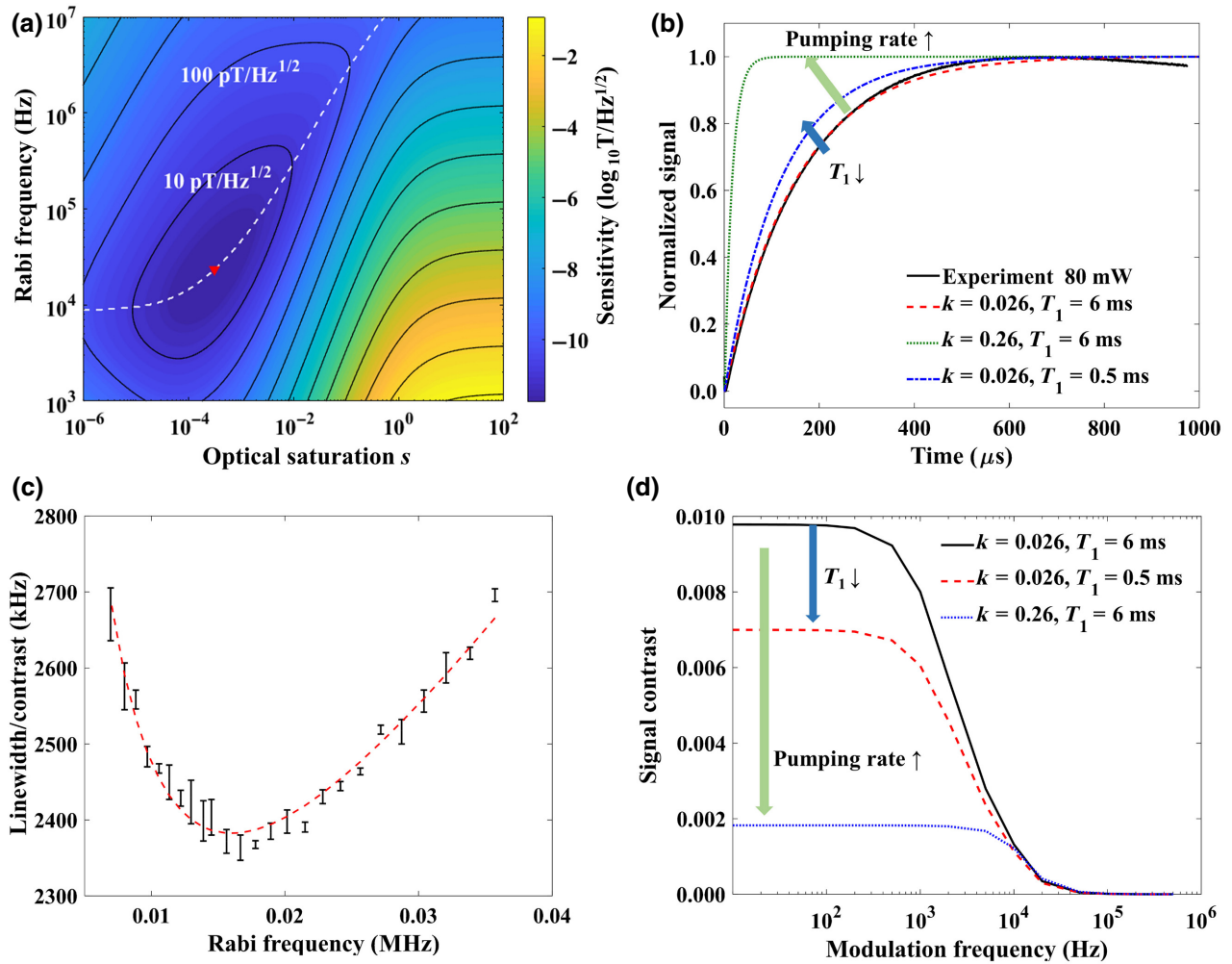


FIG. 3. (a) Optimization of theoretical shot-noise-limited sensitivity with respect to laser pumping and MW driving strength based on the cw ODMR model. $T_2^* = 8.5 \mu\text{s}$ and $T_1 = 6$ ms are the parameters used in the calculation. The dashed line shows the optimized MW strength and sensitivity for different excitation powers. The triangle marks the best theoretical sensitivity. (b) Repolarization curves for both the experimental results and the simulation, indicating the effects of the two primary parameters, the pumping rate (k in MHz) and T_1 . (c) Experimental sensitivity parameter of linewidth divided by contrast for different Rabi frequencies. The Rabi frequency for the cw ODMR method is optimized at 17 kHz. (d) Contrast of simulated cw ODMR signal for different modulation frequencies (on logarithmic scale). The pumping rate and T_1 also affect the bandwidth and contrast of the magnetometer. The diamond magnetometer has a 3-dB bandwidth of around 1.5 kHz, and the signal contrast is reduced from 1 to 20 kHz.

apply a near-optimal laser power with a pumping rate $k = 0.026$ MHz. Figure 3(b) plots the experimental fluorescence recovery curve and the simulated results for different parameters. The low pumping rate is the main reason for the millisecond repolarization time. Hence, in the low-pumping-rate case, an influence of T_1 appears in the fluorescence recovery. We use the parameter of the linewidth divided by the contrast to optimize the MW power, as plotted in Fig. 3(c). We find the optimal Ω_R to be around 17 kHz, while the applied laser power is roughly 80 mW for a beam size the same as the diamond dimensions of 0.5 mm. In order to investigate the response of the contrast to the MW modulation frequency, i.e., the magnetometer bandwidth, the calculated responses of the fluorescence

to different MW modulation frequencies are plotted in Fig. 3(d). The demodulated output magnitude of the fluorescence drops by roughly 10 times from a 1-kHz to a 20-kHz modulation frequency due to the optical-pumping dynamics and T_1 . Thus, for a MW modulation frequency higher than 1 kHz, the optimal sensitivity also degrades accordingly. The 3-dB bandwidth of the magnetometer is around 1.5 kHz at a pumping rate of 0.026 MHz. It increases to 7.4 kHz with a lower contrast when the pumping rate is 10 times higher. In addition, for a T_1 roughly 10 times shorter, the contrast also decreases. However, the 3-dB bandwidth increases only to 1.7 kHz. The SNR can be improved by MW modulation within the 3-dB bandwidth since the technical noise floor decreases with increasing

demodulation frequency. After the 3-dB frequency point, it is worth investigating whether the SNR can be further improved by reducing both the signal amplitude and the noise, which is discussed below.

III. RESULTS AND DISCUSSION

Figure 4(a) shows a comparison of the linewidth between cw ODMR, pulsed ODMR, and continuously excited pulsed ODMR at different Rabi frequencies. The diamond demonstrates a narrow cw ODMR linewidth of 28 kHz FWHM with weak MW driving, while the calculated minimum linewidth for diamond with $T_2^* = 8.5 \mu\text{s}$

is less than 20 kHz [34]. The cw ODMR results show a linewidth broadening with strong MW fields. While the cw ODMR linewidth is reduced with a reduction in MW power, the linewidths for the pulsed ODMR and the CE-pulsed-ODMR measurements stay unchanged when the width of the π pulse exceeds T_2^* . Figure 4(a) also shows that the pulsed ODMR and CE-pulsed-ODMR measurements have almost the same linewidth. In order to determine whether the contrast reduction in cw-pulsed-magnetometry degrades the sensitivity, we optimize the cw ODMR sensitivity as a benchmark for comparison with the sensitivity of a CE Ramsey measurement. We expect that the CE Ramsey measurement will combine a narrow

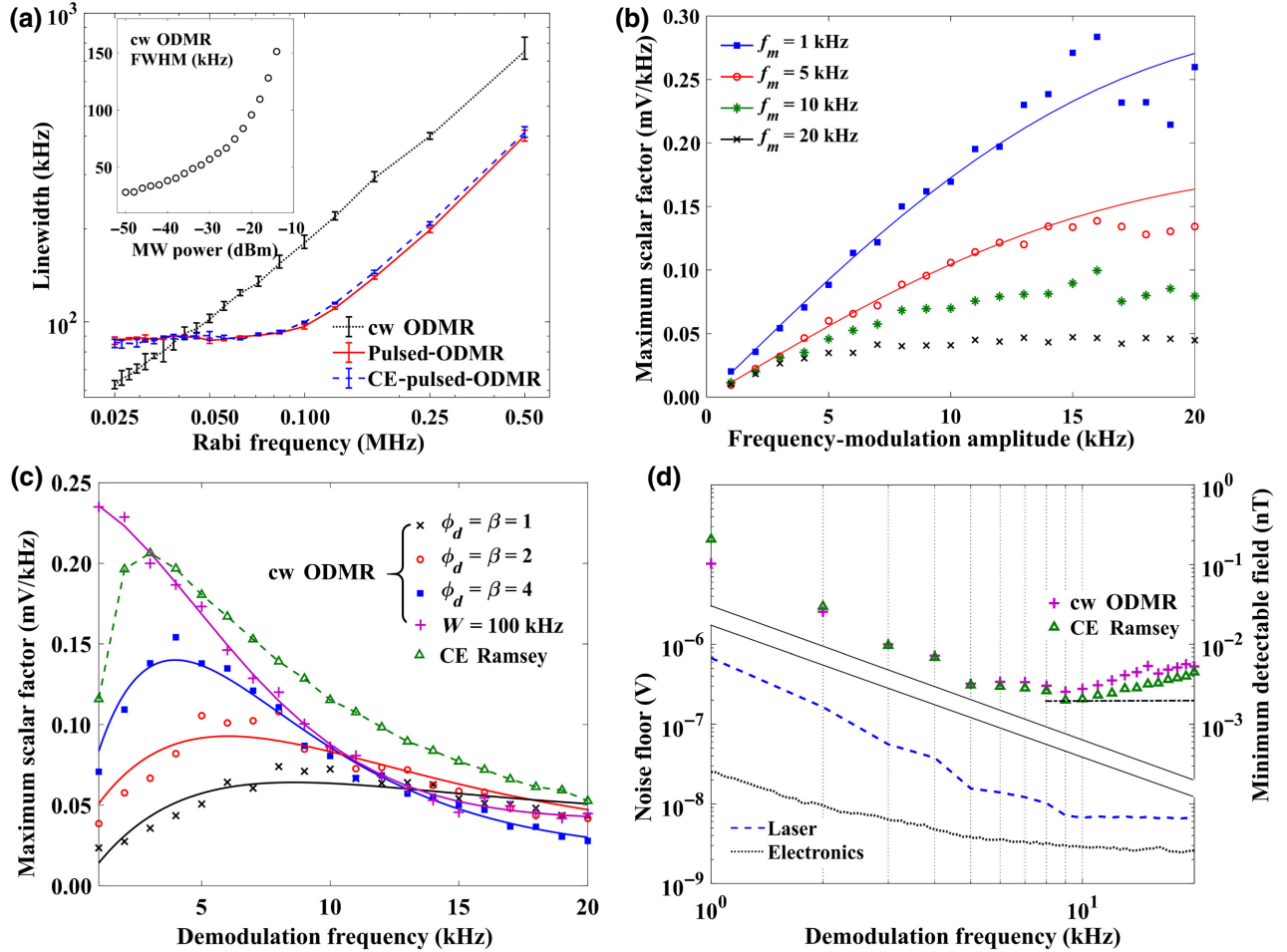


FIG. 4. (a) Linewidth measured with different Rabi frequencies by cw ODMR (black dotted line), pulsed ODMR (red solid line), and CE-pulsed-ODMR (blue dashed line). Both axes are logarithmic. The inset shows the cw ODMR linewidth for decreasing MW power. (b) Scalar factor of cw ODMR measurement with frequency-modulation (FM) signal $f_m = 1, 5, 10,$ and 20 kHz as a function of the modulation amplitude f_d . The data for $f_m = 1$ and 5 kHz fit well with the derivative of a Lorentzian lineshape. However, the fitting cannot work (it is higher than the measured results) when the bandwidth $2(f_d + f_m)$ of the modulated MW signal approaches the ODMR linewidth. (c) Comparison of scalar factors for cw ODMR (MW phase-modulated) and CE Ramsey methods for different modulation frequencies. The demodulation frequency of the CE Ramsey measurement is $1/T_{\text{seq}}$. The cw ODMR traces are plotted for different values of ϕ_d . For comparison, an extra cw ODMR curve is plotted with the FM MW signal bandwidth fixed at 100 kHz. (d) Noise floor (root-mean-square noise in volts, lower left y axis) of the electronics and demodulated laser intensity, from 1 to 20 kHz. Both axes are logarithmic. The frequency resolution of the spectra is 13.7 mHz for a 73 -s measurement time. In the upper part, the minimum detectable fields (right y axis) of the CE Ramsey and cw ODMR measurements for a bandwidth $W = 100$ kHz are plotted.

linewidth with the advantage of a good SNR due to the continuous readout. All the following measurements are based on the near-optimal laser power for the cw ODMR method, which can be easily achieved in the laboratory. Both the simulations and the experimental results show that CE Ramsey and regular Ramsey measurements yield similar results with a low-power laser [32].

The MW angular modulation is implemented as discussed in Sec. II. Either frequency modulation or phase modulation (PM) can be applied. Taking the FM MW signal as an example, the signal can be described as

$$S_{\text{FM}} = A \cos[2\pi f_0 t + \beta \sin(2\pi f_m t)], \quad (3)$$

where f_0 is the resonance frequency, f_m is the modulation frequency, and $\beta = f_d/f_m$ is defined as the modulation index, in which f_d is the FM amplitude. In the case of PM, the modulated phase term is $\phi_d \sin(2\pi f_m t)$, and the signal S_{PM} can be expressed as in Eq. (3) by replacing β with the PM amplitude ϕ_d . In applications, the FM signal is usually more precise than the PM signal due to the high frequency resolution of the instrumentation. However, the PM signal provides a more stable phase reference, which is essential when a multifrequency MW signal is applied for DR driving with lock-in detection. Another parameter that is worth discussing is the bandwidth of the modulated MW signal. The bandwidth of the modulated MW signal, i.e., the Carson bandwidth, is defined as $W_{\text{FM}} = 2(\beta + 1)f_m = 2(f_d + f_m)$, and the FM signal can be decomposed as

$$S_{\text{FM}} = A \sum_{n=-\infty}^{\infty} J_n(\beta) \sin[2\pi(f_0 + n f_m)t], \quad (4)$$

where $J_n(\beta)$ is the Bessel function of the first kind. Figure 4(b) plots the maximum scalar factor of the lock-in ODMR spectra for $f_m = 1, 5, 10,$ and 20 kHz and for f_d ranging from 1 to 20 kHz. The main reason for the decrease in the measured scalar factor with f_m is the bandwidth of the diamond magnetometer, as shown in Fig. 3(d). The lines are fitted according to the profile of the ODMR spectrum. The fitting agrees well only when $f_d + f_m$ is small and becomes poorer with increasing f_m or f_d when W_{FM} is greater than the FWHM. Figure 4(c) plots the measured maximum scalar factor as a function of increasing f_m for different values of $\phi_d = \beta$ to investigate the parameter dependence when a PM MW signal is applied. The Carson bandwidth in the case of phase modulation is $W_{\text{PM}} = 2(\phi_d + 1)f_m$. The scalar factor first rises because of the increase in the equivalent $f_d = f_m \phi_d$. For larger modulation frequencies, the scalar factor is limited mainly by the magnetometer bandwidth. An additional reduction of the signal due to the bandwidth of the modulated MW signal can be found when f_m is close to 20 kHz with $\beta = 4$ and $W_{\text{FM}} = 100$ kHz.

The scalar factor of the CE Ramsey measurement is also plotted in Fig. 4(c) for different modulation frequencies together with the cw ODMR data. It is compared with another cw ODMR measurement, in which the MW signal bandwidth is fixed and $f_d = W_{\text{FM}}/2 - f_m$ is changed according to f_m . The value of W_{FM} applied is 100 kHz to ensure the maximum modulated fluorescence signal amplitude. As depicted in Fig. 2(c), the signal measured by the CE Ramsey measurement is demodulated with the reference set by the measurement cycle time. Since the effective fluorescence signal occurs mainly at the beginning of each cycle, the LIA output is small when the demodulation frequency is low and the repolarization time is long. Thus, the scalar factor of the CE Ramsey measurement is small at the beginning and increases with the demodulation frequency. This also makes the cw ODMR signal superior to the Ramsey signal for a demodulation frequency of less than 3 kHz. When the cycle time is 250 μs , corresponding to a demodulation frequency of 4 kHz, the insufficient repolarization starts to reduce the contrast. Nevertheless, the scalar factor of the CE Ramsey measurement is still larger than that for the cw ODMR measurement over most of the range of f_m investigated. On the other hand, the high noise level from the instrumentation used in our experiments at low frequencies, as shown in Fig. 4(d), allows neither method to achieve the optimal SNR. One option for achieving better sensitivity could be to increase the laser power to several watts. According to Fig. 2(b), the repolarization time is roughly 10 times shorter when the laser power satisfies $k = 0.26$. From Fig. 3(c), the gain in contrast is about 2 times. Taking these two factors into Eq. (2), the shot-noise limit of the Ramsey measurement is roughly 6 times lower. However, a laser power of watts could introduce more technical noise, which might limit the sensitivity enhancement, and this needs to be further investigated.

We investigate the instrument noise floor by measuring the noise spectrum and plotting the calculated root-mean-square voltages at different demodulation frequencies from 1 to 20 kHz. When the setup is operated with the laser switched on and the microwave signal off-resonant, the noise is reduced by roughly 100 times from 1 to around 10 kHz. However, the signals measured by each method are reduced by only a few times, as shown in Fig. 4(c). In each measurement, the magnetometer outputs are acquired with a sampling rate of 900 Hz for 65 536 points, corresponding to a measurement time of 73 s. The minimum detected magnetic field is estimated by dividing the noise floor by the scalar factor. We plot the results calculated with these scalar factors in Fig. 4(d). This shows that the optimal demodulation frequency is 9 kHz, with a measured magnetic field noise level of 2 pT. The sensitivity value is 17 pT/ $\sqrt{\text{Hz}}$ with 1-Hz normalization. The Ramsey measurement is run with a 4-MHz Rabi frequency and a time interval $\tau_m = 6.42$ μs . Meanwhile, according to the scalar

factors shown in Fig. 4(c), the optimal cw ODMR signal is only 80% of the signal measured by the CE Ramsey method, and the optimized noise level plotted in Fig. 4(d) is roughly 2.5 pT. The values are measured and calculated for MW driving of the $|0\rangle \rightarrow |-1\rangle$ transition, hyperfine lines included. Considering the sensitivity enhancement factor of 1.3 times obtained with DR driving, we expect that the cw ODMR method will also measure a 2-pT noise level. In the measurements of the intrinsic noise of the magnetometer, batteries are used to generate a bias field with coils to achieve low magnetic field noise in the shields. However, the continuous discharging of the batteries induces a bias-field reduction during the measurements. The continuous shifting of the resonant frequency makes it difficult to run the Ramsey measurements, which require on-resonant MW pulses. The cw ODMR method is used for characterizing the intrinsic noise of the setup presented in this paper. The bias-field drift can be tracked by repeatedly sweeping the MW frequency. In order to keep the bandwidth of the modulated MW signal close to the ODMR linewidth in the measurement, the parameters applied are $f_m = 9$ kHz and $\phi_d = 2$, corresponding to $f_d = 18$ kHz and $W = 54$ kHz instead of the 100-kHz bandwidth used in Fig. 3(c).

The resonantly measured magnetic field noise spectrum is depicted in Fig. 5(a). The spectrum is calculated by taking the Fourier transform of the output of the lock-in amplifier, divided by the measured scalar factor and the gyromagnetic ratio. The magnetometer is also calibrated by applying known fields modulated at 182 kHz [32]. The magnetic field noise inside the shielding is measured with an OPM (Quspin Inc., QTFM) as a benchmark with a nominal $1\text{-pT}/\sqrt{\text{Hz}}$ sensitivity. The diamond magnetometer measures the magnetic field noise with a bias field of about 10 G, generated by coils powered by batteries. The coils are turned off when the OPM measures the noise to ensure the required bias-field range. The batteries ensure that the coil noise is lower than the residual magnetic noise inside the shields so that the OPM and the diamond magnetometer can measure the same magnetic field noise floor. The diamond magnetometer measures a noise floor of 2–3 pT for frequencies larger than 50 Hz. The noise spectrum at frequencies lower than 50 Hz is partly limited by the residual low-frequency noise inside the shields, according to the spectrum measured by the OPM. On the other hand, the discharging of the batteries is another reason for the higher noise level of the diamond magnetometer at low frequencies. The effect of the discharging can be removed by a linear fitting so that the low-frequency noise can be well characterized. In Fig. 5(b), the spectra are plotted with the discharging signal removed, and the low-frequency noise spikes are better characterized than the spectrum in Fig. 5(a). The off-resonant baseline in Fig. 5(a) marks the intrinsic noise level of the diamond magnetometer, which is 2–3 pT from 0 to 200 Hz. The noise level is consistent

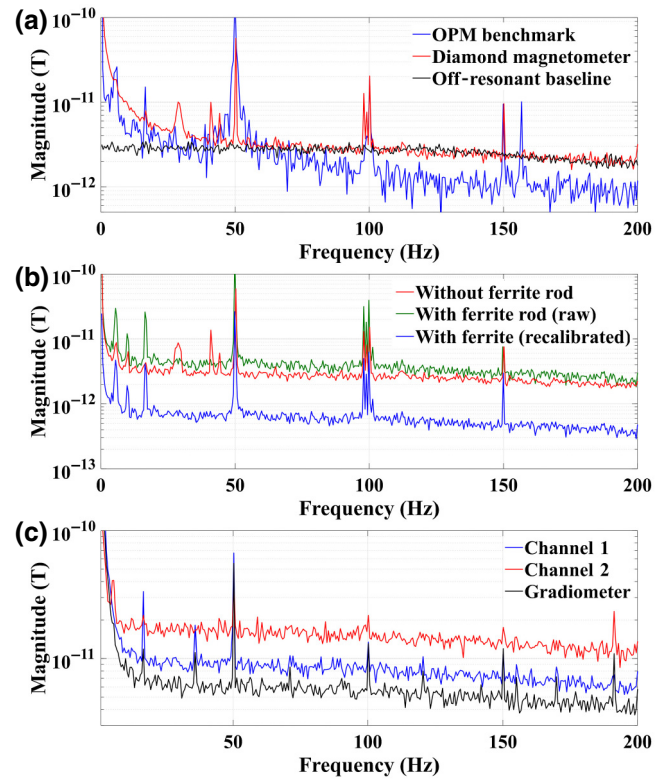


FIG. 5. (a) Magnetic field noise spectrum measured by cw ODMR method with hyperfine driving and DR driving, compared with the spectrum measured by an OPM sensor. The black line is the off-resonant baseline showing the intrinsic noise of the diamond magnetometer. With a measurement time of 73 s, all of the spectra plotted in this figure have the same frequency resolution of 13.7 mHz. The magnitudes are plotted on a logarithmic scale here and in parts (b) and (c). (b) The green and red lines show the noise spectra obtained from the direct outputs of measurements with and without a FG. The blue line shows the measured magnetic field noise calibrated using the difference between the battery-discharging signals in the two measurements. In order to see the low-frequency noise spikes, the discharging ramp of the output is removed by linear fitting before the spectral analysis. (c) Noise spectra measured by the gradiometer setup: the probe channel 1 (blue), the reference channel 2 (red), and the gradiometry signal (black) are measured. The spectrum of each single channel is measured by applying single-resonance driving, and the spectrum of the gradiometer is measured by combining the two channels and operating it with the DR driving scheme.

with the result in Fig. 4(d), which is limited by the optical noise, showing that we measure a shot-noise-limited sensitivity of $17\text{ pT}/\sqrt{\text{Hz}}$.

The most efficient way to overcome the sensitivity limit is to use a flux concentrator. The increase in sensitivity obtained from using a FC follows from a simple geometric consideration, i.e., the ratio of the areas of the surface proximal to the diamond and the distal surface defines the amplification [30]. It is also possible to use a ferrite

rod with a diameter of millimeters as a FG [39] so that the diamond can measure a remote magnetic field with a concentrated flux. Although a ferrite rod cannot provide the same flux amplification factor as a FC, the flux concentration is still remarkable due to the high magnetic permeability of the ferrite material, and the FG retains the spatial resolution. Experimentally, the magnetic field generated by the coil is guided and concentrated through the rod to the diamond. The magnetic field signal induced by the discharging of the battery is detected as the calibration signal. The discharging signal is a linearly decreasing field, and the slopes measured by the magnetometer with and without the FG are compared. With the FG, the magnetic field signal decreases 6.3 times faster than in the measurement without the FG [32]. This indicates that the flux is amplified by a factor of 6.3 times. Figure 5(b) shows a comparison of the detected magnetic field noise floors. In order to perform a better analysis of the low-frequency magnetic field noise, the discharging signal is removed from the signal traces by linear fitting before performing the Fourier transformation. Then, spikes with a frequency under 20 Hz can be seen in the spectrum; these signals come from the cooling-fan motors (typically 1000 rev/min, roughly 17 Hz) of equipment outside the shields. There is a window in the shielding cube in the direction of the FG. The magnetic noise spikes are guided through the ferrite to the diamond in the measurement. The noise floor translated from the raw output of the measurement with the FG is read as 3 pT. With a 6.3-times flux gain, the noise floor measured with the FG is estimated to be between 0.3 and 0.7 pT over the bandwidth of 20–200 Hz, as in the spectrum shown in Fig 5(b). The 1-Hz normalized spectral density of the magnetic field noise is 2.6–6 pT/ $\sqrt{\text{Hz}}$.

Using the gradiometer configuration described in Fig. 1(b), we measure the magnetic gradient-field noise of the diamond as shown in Fig. 5(c). Correspondingly, a MW signal is applied to drive the transitions $|0\rangle \rightarrow |+1\rangle$ in the probe channel (channel 1) and $|0\rangle \rightarrow |-1\rangle$ in the reference channel (channel 2). The probe channel measures a 5-pT noise level due to the driving of a single transition. The noise level of channel 2 is 10–20 pT, mainly because of the MW inhomogeneity generated by the loop antenna. Nevertheless, by combining the two signals in the DR driving scheme as shown in Fig. 2(a), the gradiometer suppresses the common-mode line shifts, and the differential signal is amplified. Each gradiometer channel can also operate with DR driving, for which four groups of MW frequencies are required. The differential signal can still be amplified by applying MW signals with a 180° phase difference between the two channels. The differential signal gain can be twice as large because the measurement is performed in two separate diamonds. In principle, the gradient-field noise increases by $\sqrt{2}$ compared with a single-channel magnetometer. Thus, the sensitivity of the

differential signal can be $\sqrt{2}$ times better. In the measurement with single-resonance driving in each channel, the measured intrinsic noise of the gradiometer is 4–6 pT in a frequency range of 20–200 Hz with a channel distance of roughly 10 cm.

IV. CONCLUSIONS AND OUTLOOK

This paper demonstrates diamond dc magnetometry and gradiometry with low optical pumping power. Fields ranging from a few picotesla to the subpicotesla level are measured within a sensing volume of 0.125 mm³. We take advantage of the narrow linewidth and the low noise floor of the lock-in detection technique, using the Ramsey method with low-power continuous excitation. With optimized parameters, the CE Ramsey measurement can achieve better sensitivity than a cw ODMR measurement. Real field measurements indicate that the intrinsic magnetic noise level of the diamond magnetometer is 2–3 pT with a 13.7-mHz frequency resolution, corresponding to a bandwidth-normalized noise spectral density of 17 pT/ $\sqrt{\text{Hz}}$. Gradiometry measurements also demonstrate a gradient-field noise of less than 10 pT with the same frequency resolution. By applying a ferrite rod with a 2-mm end diameter as a flux guide, the noise level (with the spectrum calibrated by the battery-discharging signal) can be reduced to 0.3–0.7 pT, corresponding to a bandwidth-normalized noise spectral density of 2.6–6 pT/ $\sqrt{\text{Hz}}$. For practical applications, one could combine a FG and a gradiometer to combine the advantages of sensitivity, spatial resolution, and suppression of magnetic field noise. The FG could be further optimized for higher flux gain by changing its geometry and structure, such as by changing the gap between the diamond and the FG end and by using a structure with a flux-return ferrite. Moreover, if one compromises on the spatial resolution, the setup could yield a magnetic field sensitivity of a few hundred fT/ $\sqrt{\text{Hz}}$ in the ambient environment if a flux-concentrator geometry is used. Techniques such as double quantum magnetometry [40], spin-bath driving, multiple-N-V-orientation driving, and closed-loop measurements could advance the sensitivity and stability [41,42]. With the intrinsic noise level and spatial resolution demonstrated, the diamond magnetometer can be at the forefront in a wide range of sensing applications in classical and quantum technologies.

ACKNOWLEDGMENTS

We thank Axel Griesmaier for supplying excellent photodetectors. We also thank Andrej Denisenko, Jianpei Geng, Durga Dasari, and Ayman Mohamed for fruitful discussions. We acknowledge financial support by the EU via the project ASTERIQS, by an ERC Advanced Grant (Grant No. 742610), by SMel, and by the BMBF via the project MiLiQuant and the DFG via the GRK projects 2198 and 2642. In addition, we acknowledge support by

the Japan Society for the Promotion of Science (JSPS) KAKENHI program (Grant No. 17H02751).

- [1] J. C. Allred, R. N. Lyman, T. W. Kornack, and M. V. Romalis, High-Sensitivity Atomic Magnetometer Unaffected by Spin-Exchange Relaxation, *Phys. Rev. Lett.* **89**, 130801 (2002).
- [2] J. M. Taylor, P. Cappellaro, L. Childress, L. Jiang, D. Budker, P. R. Hemmer, A. Yacoby, R. Walsworth, and M. D. Lukin, High-sensitivity diamond magnetometer with nanoscale resolution, *Nat. Phys.* **4**, 810 (2008).
- [3] H. B. Dang, A. C. Maloof, and M. V. Romalis, Ultrahigh sensitivity magnetic field and magnetization measurements with an atomic magnetometer, *Appl. Phys. Lett.* **97**, 151110 (2010).
- [4] T. Wolf, P. Neumann, K. Nakamura, H. Sumiya, T. Ohshima, J. Isoya, and J. Wrachtrup, Subpicotesla Diamond Magnetometry, *Phys. Rev. X* **5**, 041001 (2015).
- [5] N. Hinkley, J. A. Sherman, N. B. Phillips, M. Schioppo, N. D. Lemke, K. Beloy, M. Pizzocaro, C. W. Oates, and A. D. Ludlow, An atomic clock with 10–18 instability, *Science* **341**, 1215 (2013).
- [6] J. Michl, J. Steiner, A. Denisenko, A. Bülow, A. Zimmermann, K. Nakamura, H. Sumiya, S. Onoda, P. Neumann, J. Isoya, and J. Wrachtrup, Robust and accurate electric field sensing with solid state spin ensembles, *Nano Lett.* **19**, 4904 (2019).
- [7] P. Neumann, I. Jakobi, F. Dolde, C. Burk, R. Reuter, G. Waldherr, J. Honert, T. Wolf, A. Brunner, and J. H. Shim, High-precision nanoscale temperature sensing using single defects in diamond, *Nano Lett.* **13**, 2738 (2013).
- [8] T. W. Kornack, R. K. Ghosh, and M. V. Romalis, Nuclear Spin Gyroscope Based on an Atomic Comagnetometer, *Phys. Rev. Lett.* **95**, 230801 (2005).
- [9] C. Zhang, H. Yuan, Z. Tang, W. Quan, and J. C. Fang, Inertial rotation measurement with atomic spins: From angular momentum conservation to quantum phase theory, *Appl. Phys. Rev.* **3**, 041305 (2016).
- [10] X. Wu, Z. Pagel, B. S. Malek, T. H. Nguyen, F. Zi, D. S. Scheirer, and H. Müller, Gravity surveys using a mobile atom interferometer, *Sci. Adv.* **5**, eaax0800 (2019).
- [11] C. Gemmel, W. Heil, S. Karpuk, K. Lenz, Y. Sobolev, K. Tullney, M. Burghoff, W. Kilian, S. Knappe-Grüneberg, W. Müller, A. Schnabel, F. Seifert, L. Trahms, and U. Schmidt, Limit on lorentz and cpt violation of the bound neutron using a free precession $3\text{He}/129\text{Xe}$ comagnetometer, *Phys. Rev. D* **82**, 111901(R) (2010).
- [12] M. Pospelov, S. Pustelny, M. P. Ledbetter, D. F. Jackson Kimball, W. Gawlik, and D. Budker, Detecting Domain Walls of Axionlike Models Using Terrestrial Experiments, *Phys. Rev. Lett.* **110**, 021803 (2013).
- [13] E. Boto, N. Holmes, J. Leggett, G. Roberts, V. Shah, S. S. Meyer, L. D. Muñoz, K. J. Mullinger, T. M. Tierney, and S. Bestmann, Moving magnetoencephalography towards real-world applications with a wearable system, *Nature* **555**, 657 (2018).
- [14] R. Zhang, W. Xiao, Y. Ding, Y. Feng, X. Peng, L. Shen, C. Sun, T. Wu, Y. Wu, and Y. Yang, Recording brain activities in unshielded earth's field with optically pumped atomic magnetometers, *Sci. Adv.* **6**, eaba8792 (2020).
- [15] P. Maletinsky, S. Hong, M. S. Grinolds, B. Hausmann, M. D. Lukin, R. L. Walsworth, M. Loncar, and A. Yacoby, A robust scanning diamond sensor for nanoscale imaging with single nitrogen-vacancy centres, *Nat. Nano.* **7**, 320 (2012).
- [16] E. Schaefer-Nolte, F. Reinhard, M. Ternes, J. Wrachtrup, and K. Kern, A diamond-based scanning probe spin sensor operating at low temperature in ultra-high vacuum, *Rev. Sci. Instrum.* **85**, 013701 (2014).
- [17] Q. Sun, T. Song, E. Anderson, T. Shalomayeva, J. Förster, A. Brunner, T. Taniguchi, K. Watanabe, J. Gräfe, R. Stöhr, X. Xu, and J. Wrachtrup, Magnetic domains and domain wall pinning in two-dimensional ferromagnets revealed by nanoscale imaging, *Nat. Commun.* **12**, 1989 (2021).
- [18] S. Gudoshnikov, N. Usov, A. Nozdrin, M. Ipatov, A. Zhukov, and V. Zhukova, Highly sensitive magnetometer based on the off-diagonal gmi effect in co-rich glass-coated microwire, *Phys. Status Solidi A* **211**, 980 (2014).
- [19] B. Patton, E. Zhivun, D. C. Hovde, and D. Budker, All-Optical Vector Atomic Magnetometer, *Phys. Rev. Lett.* **113**, 013001 (2014).
- [20] A. Grosz, V. Mor, S. Amrusi, I. Faivinov, E. Paperno, and L. Klein, A high-resolution planar hall effect magnetometer for ultra-low frequencies, *IEEE Sens. J* **16**, 3224 (2016).
- [21] V. Shah, S. Knappe, P. D. D. Schwindt, and J. Kitching, Subpicotesla atomic magnetometry with a microfabricated vapour cell, *Nat. Photonics* **1**, 649 (2007).
- [22] C. S. Shin, C. E. Avalos, M. C. Butler, D. R. Trease, S. J. Seltzer, J. P. Mustonen, D. J. Kennedy, V. M. Acosta, D. Budker, and A. Pines, Room-temperature operation of a radiofrequency diamond magnetometer near the shot-noise limit, *J. Appl. Phys.* **112**, 124519 (2012).
- [23] D. Drung, High-performance dc squid read-out electronics, *Physica C* **368**, 134 (2002).
- [24] I. K. Kominis, T. W. Kornack, J. C. Allred, and M. V. Romalis, A subfemtotesla multichannel atomic magnetometer, *Nature* **422**, 596 (2003).
- [25] W. C. Griffith, S. Knappe, and J. Kitching, Femtotesla atomic magnetometry in a microfabricated vapor cell, *Opt. Exp.* **18**, 27167 (2010).
- [26] P. F. Wang, Z. H. Yuan, P. Huang, X. Rong, M. Q. Wang, X. K. Xu, C. Duan, C. Y. Ju, F. Z. Shi, and J. F. Du, High-resolution vector microwave magnetometry based on solid-state spins in diamond, *Nat. Commun.* **6**, 6631 (2015).
- [27] H. Zheng, J. Xu, G. Z. Iwata, T. Lenz, J. Michl, B. Yavkin, K. Nakamura, H. Sumiya, T. Ohshima, J. Isoya, J. Wrachtrup, A. Wickenbrock, and D. Budker, Zero-Field Magnetometry Based on Nitrogen-Vacancy Ensembles in Diamond, *Phys. Rev. Appl.* **11**, 064068 (2019).
- [28] A. Wickenbrock, H. Zheng, L. Bougas, N. Leefer, S. Afach, A. Jarmola, V. M. Acosta, and D. Budker, Microwave-free magnetometry with nitrogen-vacancy centers in diamond, *Appl. Phys. Lett.* **109**, 053505 (2016).
- [29] J. F. Barry, M. J. Turner, J. M. Schloss, D. R. Glenn, Y. Song, M. D. Lukin, H. Park, and R. L. Walsworth, Optical magnetic detection of single-neuron action potentials using

- quantum defects in diamond, *Proc. Nat. Acad. Sci. USA* **113**, 14133 (2016).
- [30] I. Fescenko, A. Jarmola, I. Savukov, P. Kehayias, J. Smits, J. Damron, N. Ristoff, N. Mosavian, and V. M. Acosta, Diamond magnetometer enhanced by ferrite flux concentrators, *Phys. Rev. Res.* **2**, 023394 (2020).
- [31] J. F. Barry, J. M. Schloss, E. Bauch, M. J. Turner, C. A. Hart, L. M. Pham, and R. L. Walsworth, Sensitivity optimization for nv-diamond magnetometry, *Rev. Mod. Phys.* **92**, 015004 (2020).
- [32] See Supplemental Material at <http://link.aps.org/supplemental/10.1103/PhysRevApplied.15.064075> for details of the simulation model, the continuous excitation, the magnetometer calibration, and the flux-guide-aided magnetometry.
- [33] P. Kapitanova, V. V. Soshenko, V. V. Vorobyov, D. Dobrykh, S. V. Bolshedvorskii, V. N. Sorokin, and A. V. Akimov, 3d uniform manipulation of nv centers in diamond using a dielectric resonator antenna, *JETP Lett.* **108**, 588 (2018).
- [34] A. Dréau, M. Lesik, L. Rondin, P. Spinicelli, O. Arcizet, J. F. Roch, and V. Jacques, Avoiding power broadening in optically detected magnetic resonance of single nv defects for enhanced dc magnetic field sensitivity, *Phys. Rev. B* **84**, 195204 (2011).
- [35] J. P. Tetienne, L. Rondin, P. Spinicelli, M. Chipaux, T. Debuisschert, J. F. Roch, and V. Jacques, Magnetic-field-dependent photodynamics of single nv defects in diamond: An application to qualitative all-optical magnetic imaging, *New J. Phys.* **14**, 103033 (2012).
- [36] Y. Dumeige, J.-F. Roch, F. Bretenaker, T. Debuisschert, V. Acosta, C. Becher, G. Chatzidrosos, A. Wickenbrock, L. Bougas, and A. Wilzewski, Infrared laser threshold magnetometry with a nv doped diamond intracavity etalon, *Opt. Exp.* **27**, 1706 (2019).
- [37] I. Meirzada, Y. Hovav, S. A. Wolf, and N. Bar-Gill, Negative charge enhancement of near-surface nitrogen vacancy centers by multicolor excitation, *Phys. Rev. B* **98**, 245411 (2018).
- [38] N. Aslam, G. Waldherr, P. Neumann, F. Jelezko, and J. Wrachtrup, Photo-induced ionization dynamics of the nitrogen vacancy defect in diamond investigated by single-shot charge state detection, *New J. Phys.* **15**, 013064 (2013).
- [39] W. C. Griffith, R. Jimenez-Martinez, V. Shah, S. Knaappe, and J. Kitching, Miniature atomic magnetometer integrated with flux concentrators, *Appl. Phys. Lett.* **94**, 023502 (2009).
- [40] K. Fang, V. M. Acosta, C. Santori, Z. Huang, K. M. Itoh, H. Watanabe, S. Shikata, and R. G. Beausoleil, High-Sensitivity Magnetometry Based on Quantum Beats in Diamond Nitrogen-Vacancy Centers, *Phys. Rev. Lett.* **110**, 130802 (2013).
- [41] E. Bauch, C. A. Hart, J. M. Schloss, M. J. Turner, J. F. Barry, P. Kehayias, S. Singh, and R. L. Walsworth, Ultra-long Dephasing Times in Solid-State Spin Ensembles via Quantum Control, *Phys. Rev. X* **8**, 031025 (2018).
- [42] C. Zhang, H. Yuan, N. Zhang, L. Xu, J. Zhang, B. Li, and J. Fang, Vector magnetometer based on synchronous manipulation of nitrogen-vacancy centers in all crystal directions, *J. Phys. D* **51**, 155102 (2018).